A Novel Passive Parallel Elastic Actuation Principle for Load Compensation in Legged Robots

Yifang Zhang, Jingcheng Jiang, *Graduate Student Member, IEEE*, and Nikos G. Tsagarakis

***Abstract*—This work introduces a novel parallel elastic actuation principle designed to provide torque compensation for legged robots. Unlike existing solutions, the proposed concept leverages a nitrogen N_2 gas spring combined with a cam roller module to generate a highly customizable torque compensation profile for the target leg joint. An optimization-based design approach is employed to derive the specifications of the gas spring and optimize the cam module to produce a compensation torque profile closest to the desired one. The proposed load compensation concept and related mechanism are experimentally evaluated and practically integrated into the knee joint of a two-DoF monopedal robot actuated by cycloid actuators. The experimental results demonstrate that the proposed principle can effectively generate the required compensation torque profile and achieve significant benefits for the prototyped monopedal robot system by reducing 71.92% of the additional energy consumption caused by the payload. The entire system is compact, easy to integrate, and highly customizable, enabling the creation of nonlinear torque compensation profiles as needed. The work provides a promising solution to load compensation in legged robots.**

***Index Terms*—Actuation and joint mechanisms, legged robots, mechanism design.**

I. Introduction

LEGGED robots can navigate in complex environments and various terrains by stepping actions, which often demand high actuation torque. An approach to increasing the torque capacity of actuators is including a high gear ratio reducer. However, the use of reducer leads to reduced backdrivability, increased friction losses and higher reflected inertia, compromising the actuator dynamic and force control performance [1].

An alternative approach involves employing instead a high torque/power-density motor, enabling more direct drive or low reduction ratio implementations [2], [3], [4], [5], [6]. This solution reduces the energy loss in the transmission, enhances the transparency and backdrivability and results in lower reflected inertia, which reduces impact forces and augments the actuator's resilience to impacts [1]. However, although a low gear ratio entails a notable reduction in back drive torque, it increases energy consumption to hold static loads. This drawback becomes particularly relevant in scenarios where passive gravity torque predominantly influences motion or posture. Robots employing this approach require extra energy to maintain a static squat posture to facilitate high base elevation for intricate manipulation tasks with onboard manipulators [7], [8]. For wheeled-legged robots, to enhance stability and robustness during rolling, the leg is usually maintained in a bent configuration, during which the gravitational torque of the robot body and payload is applied to joints [9], [10]. Therefore, a significant amount of energy is consumed to counteract the gravitational torque in such poses.

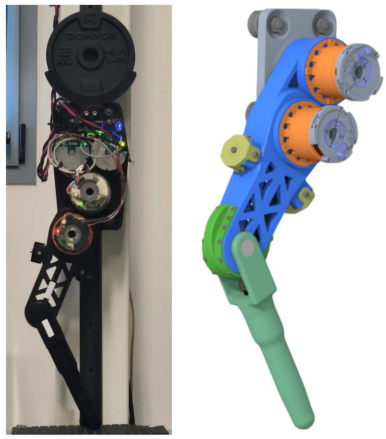

Fig. 1. The overview of the leg (Left: The prototype mounted on a vertical slider with 2 kg payload. Right: The CAD model).

To address these limitations, supplementary mechanisms incorporating elastic elements have been introduced to counteract the gravitational torque exerted on joints. Depending on whether the compensation is actively adjustable, solutions are categorized as passive or active. In active approaches, a secondary actuator is employed to adjust the pretension of the elastic element during operation [11], [12], [13]. This adjustable system significantly enhances overall system efficiency. However, the additional actuators increase mechanical and control complexity, rendering the mechanism heavier and more challenging to integrate in leg systems.

In contrast, passive solutions are characterized by compact size and easy implementation [14], [15], [16]. Nonetheless, a common limitation of passive mechanisms is the lack of

Received 12 March 2024; accepted 9 August 2024. Date of publication 22 August 2024; date of current version 12 September 2024. This article was recommended for publication by Associate Editor D. Zanotto and Editor J. P. Desai upon evaluation of the reviewers' comments. This work was supported by the European Union's Horizon Europe Framework Programme under Grant 101070596 (euROBIN). *(Corresponding author: Yifang Zhang.)*

The authors are with the Humanoids and Human Centered Mechatronics (HHCM) Research Line of Istituto Italiano Di Tecnologia (IIT), 16163 Genova, Italy (e-mail: yifang.zhang@iit.it; jingcheng.jiang@iit.it; nikos.tsagarakis@iit.it).

This letter has supplementary downloadable material available at https://doi.org/10.1109/LRA.2024.3448131, provided by the authors.

Digital Object Identifier 10.1109/LRA.2024.3448131

flexibility in design to conveniently generate desired torque compensation in a large range of motions. Due to inherent design parameters, the torque profile generated for assistance often fails to align adequately with the desired torque, requiring additional compensatory torque to counteract the spring force and achieve the desired trajectory. An alternative solution employs additional switches to control the engagement of the spring, ensuring that the spring only provides compensation within a specific range of motion [17], [18]. Nevertheless, this approach can only offer a binary switch engagement for the spring. In addition, the limited number of adjustable parameters complicates the design of the generated compensation torque profile.

To this end, we proposed a novel passive torque compensation mechanism for legged robots with following features:

- It explores a novel gas-spring and cam module mechanism, which yields high customization in fine-tuning the compensation torque profile.
- It introduces an optimization-based design approach that can automatically derive the shape of the cam module, which provides an optimized torque compensation profile that matches the desired one.
- Utilizing the proposed optimization algorithm, a spring selection method is also considered to systematically select the gas spring specifications that best match the design requirements conveniently.
- Finally, the use of a gas spring offers the advantages of easy installation and maintenance, and provides higher power density than conventional coil springs of the same size.

The rest of the letter is structured as follows. Section II introduces the design principle, modeling of the proposed mechanism, the optimization-based gas spring selection procedure, and their realization on a 2-DoF robot leg. The control method of the leg system is described in Section III. Section IV discusses the experimental validation of the proposed mechanism and corresponding controller. Section V addresses the conclusions and future work.

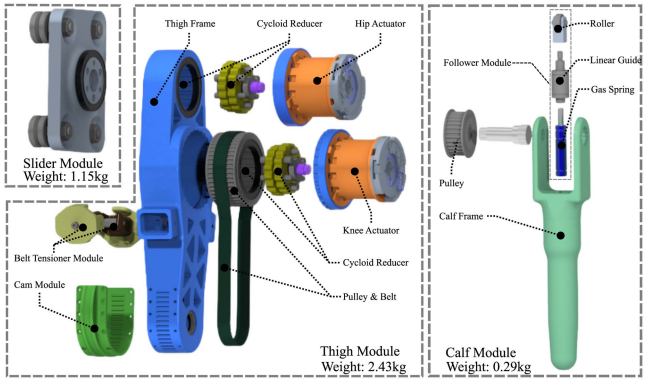

Fig. 2. The exploded view of the integrated thigh structure mechanics and actuation components.

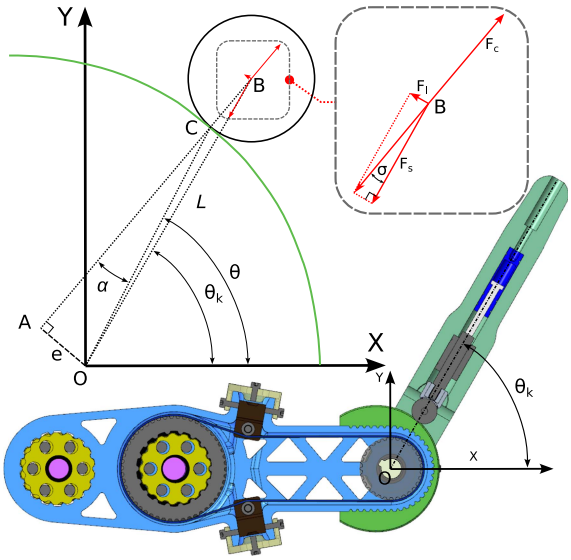

Fig. 3. The section view and the force analysis.

II. Design Principle and Implementation

At the beginning of this section, we present the modeling (Section II-A) and optimization-based (Section II-B) design approach of the load compensation mechanism. In Section II-C, the selection method of gas spring based on the desired compensation load and proposed optimization approach is introduced. In the end, the load compensation mechanism is implemented in the knee joint of a robot leg.

The detailed design of a robot leg with the load compensation mechanism is shown in Fig. 2. The mechanism contains two essential modules: a cam module (green) attached and positioned on the thigh frame (blue), and a follower module consisting of a roller, a linear guide, and a gas spring. The follower module is accommodated inside the calf frame.

A. Load Compensation Mechanism Modelling

As shown in Figs. 2 and 3, the knee joint includes a follower module embedded in the calf frame. A cam module is positioned to the thigh frame via tooth pattern on the cam module (green) and thigh frame (blue). With the increase of knee angle θ_k, the distance between the cam-follower contact point and knee rotation center is increasing. As a result, the gas spring will be compressed, and the changing rate in radial distance induces a pressure angle, which leads to an eccentricity between the normal line of the surface and the radius at the contact point. Consequently, the contact force, which has the same direction as the normal line, applied to the cam/roller will generate a compensation torque for the knee joint. Accordingly, by designing the cam profile and selecting a suitable spring, the mechanism can generate the desired assistance torque for the knee joint during knee flexion. As the design of the cam profile is highly customizable, the mechanism has the potential to generate a highly nonlinear compensation profile based on the specific requirements of the joint of leg system. First, the mechanism needs to be analyzed and modeled to reach this goal.

As shown in Fig. 3, the load compensation mechanism is modeled in a frame where its origin is located at the knee joint rotation center, and its x axis aligns with the longitude axis of the thigh. The knee angle θ_k denotes the angle between the longitude axis of the calf and the x axis of the frame. For a more

clear illustration, the essential characteristic of the mechanism is extracted and enlarged at the upper left of Fig. 3. The green line represents the profile of the cam module, while the black circle indicates the roller of the follower module. The simplified sketch shows a contact condition between the roller and cam at the knee angle θ_k.

For ease of modeling, we assume the existence of an equation that describes the cam profile. Since the cam profile of a rotary cam module is generally characterized by its angular position and radial distance, it can be represented by an unknown polar equation $\phi(\theta)$.

Then, the roller is assumed to be in contact with the cam profile at $\phi(\theta)$, and the contact point is denoted as C in Fig. 3. If at the contact point, $\phi'(\theta)$ is not 0, the direction of the reaction force of F_c, which is the contact force applied to the roller, at point C will have an offset angle α. Such offset angle will result in an eccentricity e between the direction (CA) of the contact force and the radial direction (CO) of the cam profile. By knowing the eccentricity e and the value of F_c, the torque from the compensation mechanism can be gained. However, their values can not be gained straightforwardly; the relation between system parameters is highly coupled. Nevertheless their relation with cam profile and spring properties can be derived through the following formulations.

α at θ can be expressed as

$$\alpha = \arctan \frac{\phi'(\theta)}{\phi(\theta)} \tag{1}$$

where $\phi'(\theta)$ is the first derivative of $\phi(\theta)$ and represents the changing rate of radial distance of cam profile at θ. If $\phi'(\theta)$ is equal to 0, then α and e both are 0, which results in no compensation torque being generated since the eccentricity e represents the momentum arm of F_c.

Considering that the length of CO is $\phi(\theta)$, then the eccentricity e can be derived as

$$e = \phi(\theta) \sin \alpha \tag{2}$$

According to the force analysis (shown at the top right of Fig. 3.), the contact force F_c, gas spring force F_s, and the reaction force F_l from the linear guide are balanced at the roller. F_s aligns the line BO, which connects the knee joint center O and roller center B. F_c is aligned with the normal line (CB) at contact point C, which is collinear with CA. Finally, F_s and F_l are perpendicular to each other. To this end, F_c can be derived as

$$F_c = \frac{F_s}{\cos \sigma} \tag{3}$$

where σ denotes the clamping angle between the direction of F_c and F_s. The magnitude of the spring force is determined by its initial load and the length of the gas spring stroke that has been pressed, which is equal to the change in L. Thus, the gas spring longitudinal force F_s can be written as

$$F_s = F_0 + k \cdot (L - L_0) \tag{4}$$

where F_0 and k are the initial load and the stiffness of the spring. L and L_0 represent BO length at θ and its initial length at $\theta = 0$. $L - L_0$ indicates the deflection of the spring. L in (4) can be derived using the cosines law.

$$L = \sqrt{\phi(\theta)^2 + r^2 - 2 \cdot \phi(\theta) \cdot r \cdot \cos(\pi - \alpha)} \tag{5}$$

By using also the law of cosines, σ in (3), can be obtained.

$$\sigma = \arccos\left(\frac{r^2 + L^2 - \phi^2(\theta)}{2 \cdot r \cdot L}\right) \tag{6}$$

where r represents the radius of the roller.

The compensation torque $\tau_s(\theta)$ generated by the gas spring and cam profile at θ can be formulated as

$$\tau_s(\theta) = F_c \cdot e \tag{7}$$

$\tau_s(\theta)$ is an expression containing variable θ through the cam profile $\phi(\theta)$.

However, to control the robot joint, the compensation torque needs to be expressed versus the knee angle θ_k. θ_k is not equal with θ if $\phi'(\theta)$ is not equal to 0. From the schematic in Fig. 3, the relation between θ and θ_k can be expressed as

$$\theta = \theta_k + \alpha - \sigma \tag{8}$$

By substituting (8) in (7), $\tau_s(\theta_k)$ can be obtained.

B. Optimization Based Design Approach

At the beginning of Section II-A, the cam profile is defined as an unknown function $\phi(\theta)$, determining the shape of the torque assistance profile. Observing the (6), $\phi'(\theta)$ will determine the value of the angle σ, then further affect e, which is the lever arm related to the compensation torque generated by the gas spring compression force. Thus, the choice of the expression type to consider for $\phi(\theta)$ is critical in determining the basic characteristic of the system. In this study, the form of the function is primarily chosen to be a m-order polynomial polar equation with unknown parameters u.

$$\phi(\theta) = \phi_0 + \sum_{i=1}^{m} u_i \cdot \theta^i \tag{9}$$

The choice of order m depends on the complexity of the desired torque compensation profile. A higher order m is needed for a greater non-linear profile, but results in higher demand for computational resources on the cost function. To this end, the order should be as low as possible while still satisfying the prerequisite complexity needed to generate a cam profile that can produce the desired nonlinear torque compensation profile. For the optimization task defined in Section II-C, $\phi(\theta)$ is chosen to be a third-order polynomial equation, while for a more complex problem (as shown in Section IV-B), a 12th order complexity is needed.

In (9), ϕ_0 is the initial distance between contact point C and rotation center O, whose value is defined according to mechanical constraints. Manually tuning the values of unknown coefficients is difficult as they non-linearly affect the torque profile $\tau_s(\theta)$. Therefore, we propose an optimization-based method to determine coefficients to produce a compensation torque profile fitting the desired one.

To construct the optimization problem, a desired load compensation profile is expressed as $\tau_l(\theta_k)$. Its detailed definition

depends on the user's preference. Then the $\tau_l(\theta_k)$ is converted to $\tau_l(\theta)$ to obtain an expression with the variable θ.

$$\tau_l(\theta_k) \xrightarrow{(8)} \tau_l(\theta) \tag{10}$$

The designed load compensation profile should have an optimal performance in the optimization domain which is the joint angle range to be designed with compensation. Thus, the optimization problem should be defined to gain an optimized cam profile with a minimum difference between the desired and actual compensation torque. To this end, the (10) and (7) are sampled with the same resolution step θ_r in the preferred design domain. Then, two vectors, which represent the torques generated by the load compensation mechanism $\tau_{\mathbf{s}}(\theta)$ and the desired compensation torque $\tau_{\mathbf{l}}(\theta)$ can be obtained as

$$\mathbf{T_s} = \left[\tau_s\left(\theta_{\min}\right), \tau_s(\theta_{\min} + \theta_r), \ldots, \tau_s\left(\theta_{\min} + n * \theta_r\right)\right] \tag{11}$$

$$\mathbf{T_l} = \left[\tau_l(\theta_{\min}), \tau_l(\theta_{\min} + \theta_r), \ldots, \tau_l(\theta_{\min} + n * \theta_r)\right] \tag{12}$$

n is defined as

$$n \in \left[0, \frac{\theta_{\max} - \theta_{\min}}{\theta_r}\right] \tag{13}$$

where $\theta_{\max}$ and $\theta_{\min}$ represent the maximum and minimum angular positions of the cam profile in the polar coordinate, which is a user-defined design domain. It is important to note that, due to the relationship in (8), the design range should be slightly larger to encompass the desired knee motion range. Then the error vector $\mathbf{E}_\tau$, which represents the difference between the elements in $\mathbf{T_s}$ and $\mathbf{T_l}$, can be obtained. The cost function of the optimization problem is constructed as

$$\begin{aligned} \min_{u} \quad & J = {\mathbf{E}_\tau}^T \cdot \mathbf{E}_\tau \\ \text{s.t.} \quad & 0 \leq L - L_0 \leq l_s \end{aligned} \tag{14}$$

that attempts to minimize the sum of the errors' squares by finding the optimal u, the unknown coefficients of (9). The constraint regulates the moving range of the gas spring rod in its stroke. Moreover, the following parameters from commercial parts need to be predefined in the optimization problem.

- r - The roller radius.
- F_0 - The initial force of the gas spring.
- k - The stiffness of the gas spring.
- l_s - The stroke of the gas spring.

The optimization problem is constructed with CasADi and solved with a nonlinear programs solver IPOPT [19]. After the optimization, by substituting the optimal parameters u to (9), the corresponding optimal cam profile $\phi(\theta)$ can be obtained.

C. Gas Spring Selection

To perform the optimization introduced in the previous section, we need to define parameters of the spring. The spring selection needs to consider a designed load compensation demand. Here, we choose the most common scenario, where we aim to compensate for the gravity torque generated by an extra payload mounted on top of the hip joint when the momopedal leg (as shown in Fig. 2) performs a vertical squat. In the following sections, the actuation system and corresponding controller

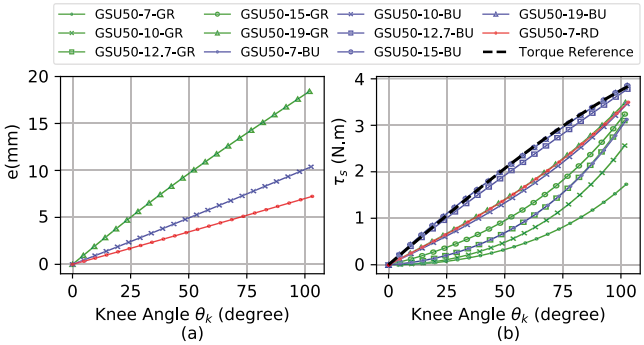

Fig. 4. (a) The eccentricity e lines are formed by the optimized cam profiles with gas spring GSU50-19-GR, GSU50-10-BU, and GSU50-7-RD. (b) Suspension torque profile τ_s is formed by the optimized cam profile with different gas springs.

will be developed for this leg system and used to evaluate the benefits that the torque compensation mechanism confers upon the monopedal robot system. Then, the torque induced by the extra payload at the knee joint, $\tau_{lk}(\theta_k)$, can be computed as

$$\tau_{lk}(\theta_k) = w \cdot g \cdot l_t \cdot \sin\frac{\theta_k}{2} \tag{15}$$

where w denotes the payload weight, and l_t indicates the thigh link length (The thigh and calf links are both 250 mm in length). For the selection of the elastic element, we consider w to be 2 kg. Since the torque profile in this scenario is symmetric to the axis x, the optimization can be simplified by shrinking the design domain to half of the knee motion range, which can further reduce computational resource consumption. To this end, $\theta_{\min}$ and $\theta_{\min}$ are set as 0° and 110° respectively. To be noted, the desired load compensation profile can also be the gravity torque for the robot's body weight. Here, we use the additional payload for the convenience of comparison in experiments.

As shown in Fig. 2, the follower includes a spring integrated into the calf. To minimize the inertia of the calf link, N_2 gas springs appear a better choice than conventional coil springs of similar size since they typically have a much higher power density. Their simpler installation permits compact integration, which further reduces the system weight [20].

Several interacting parameters constrain the selection of the gas springs. As we can observe from (1), a high value of $\phi'(\theta)$ will result in a high eccentricity, which leads to a higher rate of change in the displacement of the rod of the gas spring. This means that to achieve the same compensation torque profile, a weaker (lower initial force and spring factor) gas spring needs a more significant stroke than a stronger gas spring. For instance, the gas springs GSU50-19-GR, GSU50-10-BU, and GSU50-7-RD produce nearly identical compensation torque profiles τ_s (Fig. 4(b)), while the eccentricity e (Fig. 4(b)) formed with weaker springs are more significant. As a result, a weaker spring needs a longer stroke. However, a strong gas spring will increase the radial load applied to the bearings and the structural load to the body parts. In this work, considering the size and load capacity of the gas springs, GSU serial gas springs from MISUMI are chosen for the optimization study. Optimizations are performed considering gas springs with a stroke lower than 19 mm (larger strokes will cause the parts to have a larger size and

weight) and a maximum spring force lower than 500 N (taking into account the strength of 3D printing material ABS). The simulation results of the gas spring load compensation mechanism are plotted in Fig. 4. For each spring, the cam profile is optimized to minimize the difference between extra load torque and the compensation torque generated by the gas spring. In Fig. 4, the $green$, $blue$, and red colors denote the results of springs with 130, 250, and 380 N initial load, respectively. The markers, dot, star, square, circle, and triangle denote the gas springs with strokes 7, 10, 12.7, 15, and 19 mm, respectively. The supplier does not provide the spring stiffness profile. However, given that the stroke of these gas springs is significantly smaller than their body length, the volume of the pressure chamber undergoes only minor changes. Consequently, based on the ideal gas law, we presume they operate within a range exhibiting minimal nonlinear properties. To this end, the N_2 gas spring is simplified as a linear spring model with a constant stiffness of k assumed.

$$k = \frac{F_{\max} - F_{initial}}{l_s} \tag{16}$$

The simulation results are illustrated in Fig. 4(b). The load compensation profiles of GSU50-15-BU and GSU50-19-BU almost overlap with the knee torque profile (the black dashed line) caused by 2 kg payload. As the gas spring with a shorter stroke is lighter and smaller, GSU50-15-BU is selected, and the corresponding optimized cam profile is given by the optimization as

$$\phi(\theta) = 35 - 0.0018 \cdot \theta + 5.14 \cdot \theta^2 - 0.71 \cdot \theta^3 \tag{17}$$

where θ has unit in rad while $\phi(\theta)$ is in mm.

D. Actuation System Design

A 2-DoF (hip and knee) robot leg with the load compensation mechanism integrated at the knee joint (as shown in Fig. 2) is developed for the experimental validation. The hip actuator is axially aligned with the hip joint, while the knee actuator is lifted to be as close as possible to the hip to reduce the system inertia. In our design (Fig. 2), both cycloidal disc pins are affixed to their parent link and function as the stator, while the outer ring pins serve as the rotor. Notably, for the thigh actuator's reducer, the entire thigh frame constitutes an integral part of the reducer, with the ring pins seamlessly integrated into the inner wall of the thigh frame. For the knee actuator, the ring pins of the cycloid reducer are integrated into a 3D-printed pulley. This tight integration of the cycloid reducer components with the structural body of the thigh results in the reduction of the overall size and mass of the leg system. The subsequent transfer of power is accomplished through a belt transmission system characterized by a 0.6:1 gear ratio. The incorporation of this belt transmission system serves the purpose of optimizing the placement of the knee actuator in close proximity to the hip joint, thereby ameliorating inertial effects at the distal extremity of the system. The selection of a 0.6:1 ratio is primarily predicated upon a thoughtful equilibrium between size, weight, and 3D printing tolerance.

To ensure the leg can perform designed motions for experimental validations, actuators at the knee and hip joint should be able to provide sufficient torque. In the presented leg robot prototype, the actuation drives are realized with the combination of frameless motor TBM(S)-6025-B from Kollmorgen and highly integrated cycloid reducers. Given the selected actuator, a simulation study was performed to understand the demanding torque of each joint, based on which to select the gear ratio of the custom-designed cycloid reducer. In the simulation, the leg performs a vertical squat along the vertical slider, Fig. 1, while carrying a 2 kg payload. The hip and knee joints are executing a sinusoidal trajectory shown in Fig. 5. The simulation was conducted using the PINOCCHIO robotic library [21], and the results are plotted in Fig. 5.

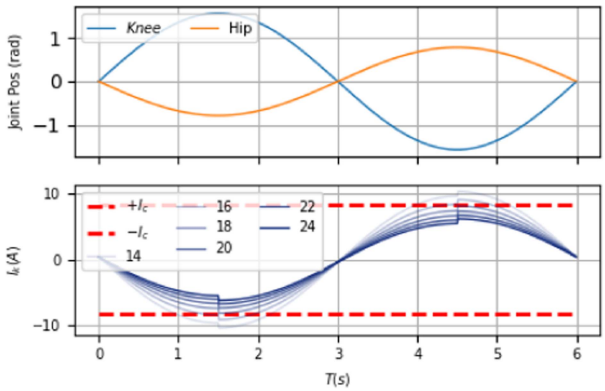

Fig. 5. Joint trajectory and motor current of different reduction ratios in the simulation.

The plot shows the current required to drive the motor module through one cycle of the sinusoidal motion with various reduction ratios, ranging from 14:1 to 24:1 (The small step in each current curve is caused by the switching of the friction force direction when the motion direction is turned.). In the plot, two red lines indicate the maximum continuous current (±8.25 A) of the motor. It can be observed that the knee joint actuator with the ratio of 18:1 just reaches the red line (Since the motion in the simulation is not energy-intensive, the continuous current is used as the design criterion to allow for some adaptability in handling impacts and energy-intensive motions in actual conditions.). Therefore, for the knee actuator, the reducer is designed with an 18:1 reduction ratio, while the overall reduction ratio reaches 10.8:1 from the motor to the joint. Additionally, during vertical squat motions, the center of mass (COM) of the payload will remain on top of the hip joint's rotation axis. Thus, the torque and speed requirements of the hip joint are less demanding than those of the knee joint. Consequently, the hip joint actuator makes use of the same cycloid reducer, which also has the benefit of minimizing the number of different 3D printing parts. An experimental evaluation of the actuator efficiency is conducted. Based on the experimental data, the efficiency, including both electronic and mechanical losses, of the actuator is computed and plotted in Fig. 6.

The ultimate design is portrayed in Fig. 2. Finally, all non-standard parts were realized via 3D printing using ABS materials, including the thigh frame, calf frame, pulleys, cycloid disks, and cam modules, ensuring a fast prototype of the leg and validation of the proposed load compensation mechanism.

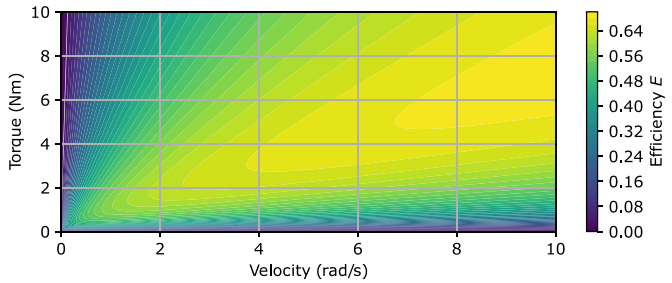

Fig. 6. The efficiency E including electronic and mechanical losses of the designed actuator.

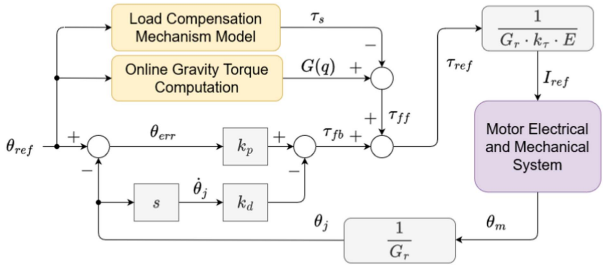

Fig. 7. The control schematic depicting the PD position controller and feedforward components.

III. Leg Control

A. Sensing and Instruments

For the control of actuators of the legs joints, two Renishaw encoders (MB049) are attached to the motor side of the two actuators to provide motor position θ_m feedback for the PD position controller. The motor current is measured with sensors integrated into the motor drive stacks. An embedded PC (COM Express) running a real-time system Xenomai 3 and an EtherCAT master module enabled real-time control and communication through EtherCAT with the joint actuators and sensors. The communication bandwidth was set at 1 kHz.

B. Controller Design

As shown in Fig. 7, the outer control loop implements a PD position regulator to generate a demanding torque τ_{fb}.

$$\tau_{fb} = K_p \cdot \theta_{err} + K_d \cdot \dot{\theta}_j \tag{18}$$

where K_p and K_d are the proportional and derivative gains of the PD controller. θ_j represents the joint position derived from the motor position θ_m considering the gear ratio G_r.

$$\theta_j = \frac{\theta_m}{G_r} \tag{19}$$

To improve the trajectory tracking performance, a feedforward term is added to the demanding torque τ_{fb} generated by the PD position controller. This term is derived from an online gravity torque computation module and load compensation module that both take the position reference as input and output the static gravity torque and compensation torque, respectively. Thus, the feedforward torque reference τ_{ff} is computed as

$$\tau_{ff} = \boldsymbol{G(q)} - \tau_s \tag{20}$$

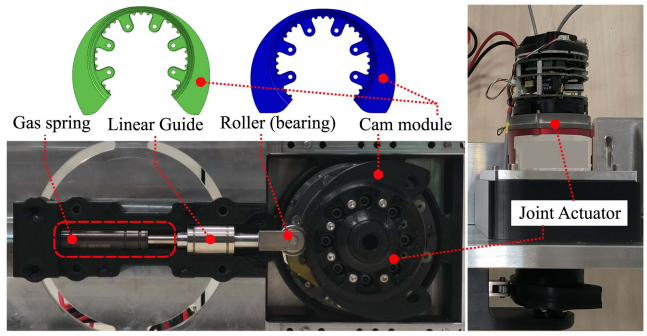

Fig. 8. The experimental setup for evaluation the load compensation mechanism.

The leg is modeled with a URDF file, and $\boldsymbol{G(q)}$ is online computed with the function $computeStaticTorque$ of the PINOCCHIO library [21]. τ_s is the compensation torque, which will be directly set to zero if the cam module is removed. The joint torque reference τ_{ref} can be obtained as

$$\tau_{ref} = \tau_{fb} + \tau_{ff} \tag{21}$$

The current reference I_{ref} of the actuator is then obtained with τ_{ref} and actuator's parameters.

$$I_{ref} = \frac{\tau_{ref}}{G_r \cdot k_\tau \cdot E} \tag{22}$$

where G_r is the overall gear ratio, k_τ is the motor torque constant and E is the efficiency of entire transmission mechanism.

IV. Experimental Validation

A. Experimental Design

Two experiments were performed to evaluate the functionality of the load compensation mechanism. The first experiment aims to evaluate the performance of the torque compensation mechanism on a testbed, while the second experiment aims to assess the advantages conferred by the designed torque compensation module to the monopedal robot system.

B. Load Compensation Mechanism Evaluation Experiments

As shown in Fig. 8, a testbed was developed to evaluate the load compensation mechanism. The cam module is attached to the link (output) side of an actuator, which is equipped with a strain gauge-based torque sensor. The N_2 gas spring, linear guide, and roller are integrated into a base with the same configuration as in the calf module (Fig. 2). The green cam module (Fig. 8) is printed with the optimized profile (17). Additionally, to prove that the proposed solution can generate compensation for a highly nonlinear torque profile, a highly nonlinear load profile was also generated and plotted (Black dashed line) in Fig. 10(b). The highly nonlinear profile is used as input of the optimization problem to derive an optimized cam profile. Correspondingly, a higher order (9) is needed for providing sufficient adaptability to generate an optimized cam profile that can provide the highly nonlinear compensation torque profile. To this end, the polynomial equation of the optimized cam profile

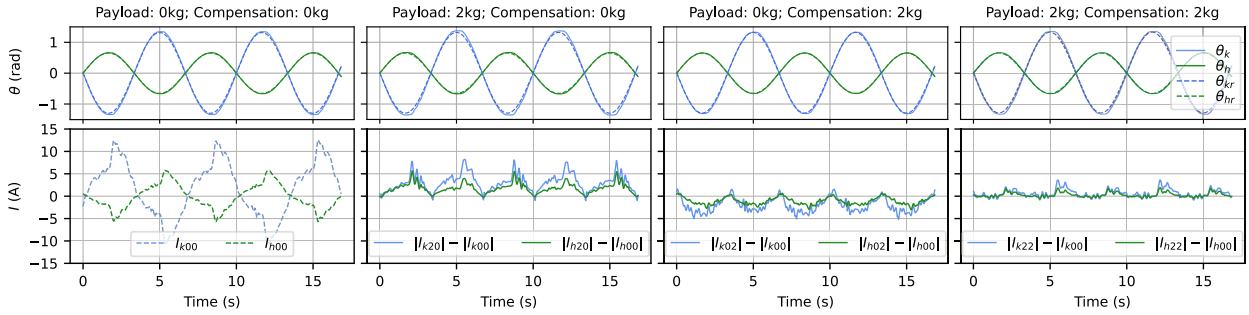

Fig. 9. Experimental result of monopedal robot experiments.

was extended to the 12th order.

$$\begin{aligned}\phi(\theta) = \; & 35 + 0.00076 \cdot \theta + 9.49 \cdot \theta^2 - 0.65 \cdot \theta^3 - 0.31 \cdot \theta^4 \\ & - 49.31 \cdot \theta^5 + 89.25 \cdot \theta^6 - 24.6 \cdot \theta^7 - 68.98 \cdot \theta^8 \\ & + 81.21 \cdot \theta^9 - 39.49 \cdot \theta^{10} + 9.35 \cdot \theta^{11} - 0.89 \cdot \theta^{12}\end{aligned} \tag{23}$$

The blue cam in Fig. 8 is constructed with profile (23).

During the experiments, as the link side of the actuator rotates, the eccentric surface of the cam module causes the contact force with the roller (bearing) to generate torque on the link side. The embedded torque sensor measures the torque while the link side encoder records the link side position. The actuator repeats the same smooth trajectory for both cam modules with an angle range from 0° to 100°. To evaluate the performance of the mechanism under different velocities, the trajectory is completed within different time periods of 1, 2, 3, and 4 seconds. As shown in Fig. 10, measured torque profiles at different motion speeds demonstrate nearly identical torque curves, close to the desired one, which indicates that the proposed optimization-based design approach has the capability to generate highly nonlinear torque profiles as needed.

C. Monopedal Robot Experiments

A vertical squat motion is conducted with the 2-DoF monopedal prototype. The joint trajectory is the same as that in the simulation (Fig. 5). The cam modules shown in Fig. 2 were printed according the optimized profile (17). Four sets of experiments are conducted with different conditions: i) without payload and without compensation, ii) with payload and without compensation, iii) without payload and with compensation, and iv) with payload and with compensation.

Experimental results are shown in Fig. 9 with [*Payload: * kg; Compensation: * kg*] on top of the plot indicating the configuration. The **Payload** indicates the applied weight, while the **Compensation** indicates the applied compensation cam module. The first row of each experiment's plot shows the reference (θ_{kr} and θ_{hr}) and measured (θ_k and θ_h) position of knee and hip joints. To facilitate comparison in torque compensation and energy consumption, the measured motor current $|I_{xy}|$ of the different load and compensation conditions is compared with the measured current $|I_{00}|$ of the no-load and no-compensation condition. The current difference I_d is computed and plotted in the second row of each experiment's plot. As the difference of

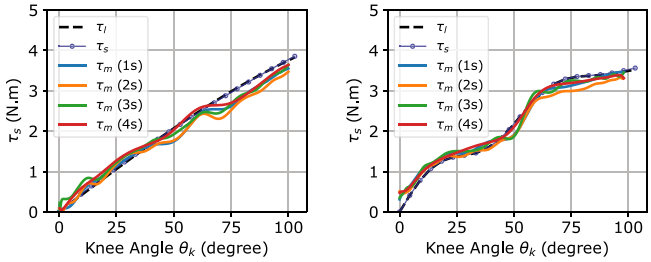

(a) (b)

Fig. 10. Torque curves (black dashed curve: desired torque profile; blue dotted curve: simulated torque with optimized cam; solid curves: measured torque for trajectories of different duration.)

non-payload and non-compensation condition to itself is always 0, In the first plot, instead of I_d, the raw I_{00} of this condition is plotted.

$$I_d = |I_{xy}| - |I_{00}| \tag{24}$$

Negative I_d indicates lower actuator torque than that of the no-load and no-compensation condition, while positive I_d indicates the opposite.

In all experiments, the reference and measured joint position almost overlap with minimal tracking errors, verifying the effectiveness of the designed controller regardless of the different payload and compensation conditions. In the result of [*Payload:* 2 *kg; Compensation:* 0 *kg*], I_d is positive, as a consequence of the resulted in increased torques in the joins of the leg. In contrast, in the result of [*Payload:* 0 *kg; Compensation:* 2 *kg*], I_d is negative since the gravity payload of the leg itself is partially compensated and less torque is required to perform the same motion.

In the plot of [*Payload:* 2 *kg; Compensation:* 2 *kg*], I_d is significantly lower than I_d in [*Payload:* 2 *kg; Compensation:* 0 *kg*], demonstrating that the compensation module reduces the effect of the payload on the system. The overall energy consumption of the system over the period of plotting (Fig. 9) was computed indicating energy consumption (including both electronic consumption and mechanical consumption) levels of 311.77 J, 722.28 J, 153.94 J, and 427.05 J for the [*Payload:* 0 *kg; Compensation:* 0 *kg*], [*Payload:* 2 *kg; Compensation:* 0 *kg*], [*Payload:* 0 *kg; Compensation:* 2 *kg*], and [*Payload:* 2 *kg; Compensation:* 2 *kg*] conditions, respectively. The use of the load compensation module reduces 50.62% of the system energy

consumption in non-payload condition, and 71.92% of the additional energy consumption caused by the 2 kg payload. It should be noted that the peak velocity of the actuator at the output side is approximately 0.89 rd/s, indicating that the actuator operates in a low-efficiency zone (as shown in Fig. 6). A significant portion of energy is dissipated due to electronic losses. Therefore, the energy savings from the load compensation module not only reduce high percentage of mechanical power consumption but also electronic power consumption.

These experimental results demonstrate that the proposed mechanism effectively provides torque compensation to the robot joint, generating significant benefits in reducing the energy consumption of the robotic system.

V. Conclusion and Future Work

This work introduced a novel joint torque compensation principle that is implemented with the combination of a N_2 gas spring and a cam profile module. The proposed mechanism permits the production of highly nonlinear load compensation profiles for the target joint. To achieve this, we proposed an optimization-based design approach, which can easily customize optimized cam profiles, minimizing the overall error between the generated and desired torque compensation profiles. We also introduced a gas spring selection method, which makes use of the cam module optimization algorithm.

It has been experimentally demonstrated that the mechanism can generate the desired compensation torque. Additionally, the proposed optimization-based design approach can produce a cam profile for highly nonlinear torque compensation. In the experiments with the monopedal robot, it has been shown that the optimized cam module and selected gas spring can effectively compensate the gravitational torque due to the mass of the robot itself and that of the additional payload. The designed compensation module reduces 50.62% of the system energy consumption in non-payload condition, and 71.92% of the additional energy consumption induced by the 2 kg payload. The proposed compensation mechanism significantly reduces the energy consumption of the monopedal robot.

However, with the current monopedal robot setup, validating the load compensation mechanism is not feasible for more complex and realistic operating scenarios, such as walking on varied terrains at different speeds. To address this limitation, our forthcoming activities will include prototyping the full quadruped system using lightweight metal and investigating the characteristics and performance of the mechanism during more intensive and dynamic motions, such as jumping and fast cyclic trajectories. Additionally, the energy benefits that the mechanism brings to the entire robot system in varied and challenging environments will be assessed.

References

[1] J. Pratt and B. Krupp, "Series elastic actuators for legged robots," *Proc. SPIE*, vol. 5422, pp. 135–144, 2004.

[2] B. Xing et al., "The moco-minitaur: A low-cost direct-drive quadruped robot for dynamic locomotion," in *Proc. Intell. Robot. Appl.: 14th Int. Conf.*, X.-J. Liu, Z. Nie, J. Yu, F. Xie, and R. Song, Berlin, Germany, 2021, pp. 378–389.

[3] A. De and D. E. Koditschek, "Parallel composition of templates for tail-energized planar hopping," in *Proc. IEEE Int. Conf. Robot. Automat.*, 2015, pp. 4562–4569. doi: 10.1109/ICRA.2015.7139831.

[4] S. Seok et al., "Design principles for energy-efficient legged locomotion and implementation on the MIT cheetah robot," *IEEE/ASME Trans. Mechatron.*, vol. 20, no. 3, pp. 1117–1129, Jun. 2015.

[5] B. Katz, J. D. Carlo, and S. Kim, "Mini cheetah: A platform for pushing the limits of dynamic quadruped control," in *2019 IEEE Int. Conf. Robot. Automat.*, 2019, pp. 6295–6301.

[6] P. M. Wensing, A. Wang, S. Seok, D. Otten, J. Lang, and S. Kim, "Proprioceptive actuator design in the MIT cheetah: Impact mitigation and high-bandwidth physical interaction for dynamic legged robots," *IEEE Trans. Robot.*, vol. 33, no. 3, pp. 509–522, Jun. 2017.

[7] J.-P. Sleiman, F. Farshidian, M. V. Minniti, and M. Hutter, "A unified MPC framework for whole-body dynamic locomotion and manipulation," *IEEE Robot. Automat. Lett.*, vol. 6, no. 3, pp. 4688–4695, Jul. 2021.

[8] I. Dadiotis, A. Laurenzi, and N. Tsagarakis, "Trajectory optimization for quadruped mobile manipulators that carry heavy payload," in *2022 IEEE-RAS 21st Int. Conf. Humanoid Robots*, 2022, pp. 291–298.

[9] V. S. Medeiros, E. Jelavic, M. Bjelonic, R. Siegwart, M. A. Meggiolaro, and M. Hutter, "Trajectory optimization for wheeled-legged quadrupedal robots driving in challenging terrain," *IEEE Robot. Automat. Lett.*, vol. 5, no. 3, pp. 4172–4179, Jul. 2020.

[10] X. Zhao, Y. You, A. Laurenzi, N. Kashiri, and N. Tsagarakis, "Locomotion adaptation in heavy payload transportation tasks with the quadruped robot centauro," in *2021 IEEE Int. Conf. Robot. Automat.*, 2021, pp. 5028–5034.

[11] G. Mathijssen, D. Lefeber, and B. Vanderborght, "Variable recruitment of parallel elastic elements: Series–parallel elastic actuators (SPEA) with dephased mutilated gears," *IEEE/ASME Trans. Mechatron.*, vol. 20, no. 2, pp. 594–602, Apr. 2015.

[12] W. Roozing, Z. Li, G. Medrano-Cerda, D. Caldwell, and N. Tsagarakis, "Development and control of a compliant asymmetric antagonistic actuator for energy efficient mobility," *IEEE/ASME Trans. Mechatron.*, vol. 21, no. 2, pp. 1080–1091, Apr. 2016.

[13] Z. Ren, W. Roozing, and N. G. Tsagarakis, "The eLeg: A novel efficient leg prototype powered by adjustable parallel compliant actuation principles," in *2018 IEEE-RAS 18th Int. Conf. Humanoid Robots*, 2018, pp. 1–9.

[14] P. Arm et al., "SpaceBok: A dynamic legged robot for space exploration," in *2019 IEEE Int. Conf. Robot. Automat.*, 2019, pp. 6288–6294.

[15] S. Shirata, A. Konno, and M. Uchiyama, "Design and evaluation of a gravity compensation mechanism for a humanoid robot," in *2007 IEEE/RSJ Int. Conf. Intell. Robots Syst.*, 2007, pp. 3635–3640.

[16] A. A. Badri-Spröwitz, A. Tuleu, M. Vespignani, M. Ajallooeian, E. Badri, and A. Ijspeert, "Towards dynamic trot gait locomotion: Design, control, and experiments with cheetah-cub, a compliant quadruped robot," *Int. J. Robot. Res.*, vol. 32, pp. 932–950, 2013.

[17] X. Liu, A. Rossi, and I. Poulakakis, "A switchable parallel elastic actuator and its application to leg design for running robots," *IEEE/ASME Trans. Mechatron.*, vol. 23, no. 6, pp. 2681–2692, Dec. 2018.

[18] F. Nan, H. Kolvenbach, and M. Hutter, "A reconfigurable leg for walking robots," *IEEE Robot. Automat. Lett.*, vol. 7, no. 2, pp. 1308–1315, Apr. 2022.

[19] J. Andersson, J. Gillis, G. Horn, J. Rawlings, and M. Diehl, "Casadi: A software framework for nonlinear optimization and optimal control," *Math. Program. Comput.*, vol. 11, pp. 1–36, 2018.

[20] "Gas spring for stamping and injection molding," Accessed: Sep. 14, 2023. [Online]. Available: https://www.pascalenginc.com/products/gas-spring/

[21] J. Carpentier et al., "Pinocchio: Fast forward and inverse dynamics for poly-articulated systems," 2021. [Online]. Available: https://stack-of-tasks.github.io/pinocchio